7.3 THE EFFECT OF DEPOSITION RATE, MISCUT ANGLE AND ORIENTATION ON Fe-$Y_2Ti_2O_7$ INTERFACES: IMPLICATIONS TO THE DEVELOPMENT AND OPTIMIZATION OF NANOSTRUCTURED FERRITIC ALLOYS —

T. Stan, Y. Wu, and G. R. Odette (University of California, Santa Barbara)

OBJECTIVE

The objective of this work is to better understand and characterize the interfaces between Y-Ti-O nano-features (NF) and the bcc Fe-Cr ferrite matrix in nanostructured ferritic alloys (NFA).

SUMMARY

The smallest 2-3 nm features in nanostructured ferritic alloys (NFA) are $Y_2Ti_2O_7$ complex oxide cubic pyrochlore phase. The interface between the bcc Fe-Cr ferrite matrix and the fcc $Y_2Ti_2O_7$ plays a critical role in the stability, strength and damage tolerance of NFA. To complement other characterization studies of the actual nano-features, mesoscopic interfaces were created by electron beam deposition of a thin Fe layer onto {111} and {100} $Y_2Ti_2O_7$ bulk single crystal surfaces. Cross-section high resolution TEM was used to characterize details of the interfaces, which ranged from being atomically sharp to more diffuse interface zones that, in some cases, included a thin metallic oxide MO_x layer. The fast deposited polycrystalline Fe layer on the 5 degree miscut {111} $Y_2Ti_2O_7$ sample has the Nishiyama-Wasserman orientation relationship: $\{110\}_{Fe}||\{111\}_{Y2Ti2O7}$ and $<001>_{Fe}||<110>_{Y2Ti2O7}$. Fe grains on the well-oriented {111} $Y_2Ti_2O_7$ sample have nano-grains at the interface. The grains on the {100} $Y_2Ti_2O_7$ sample were {110} textured but had no in-plane orientation relationship with the sample. We recognize that the mesoscopic interfaces may differ from those of the embedded NF, but the former will facilitate characterization and investigations of the functionality of controlled interfaces, such as interactions with point defects and helium.

BACKGROUND

Materials in fission and fusion reactor environments are subject to high temperatures, large time-varying stress, chemically reactive environments, and intense radiation fields [1]. Helium that is produced by transmutation reactions interacts with displacement damage to drive complex microstructural evolutions. Most notably, helium is insoluble in steels and precipitates as gas bubbles that act as formation sites for both growing voids and creep cavities, while also embrittling grain boundaries over a wide range of temperatures. NFA have been found to be radiation tolerant since they contain an ultrahigh density of Y-Ti-O nanofeatures (NF) that trap He in harmless [2], fine-scale bubbles, suppressing void swelling and embrittlement. NF also provides high stable sink densities for defect annihilation and high creep strength due to dislocation pinning [2].

Most previous TEM studies have indicated that the NF is complex oxides, primarily fcc cubic pyrochlore $Y_2Ti_2O_7$. For example, scanning transmission electron microscopy (STEM) energy dispersive X-ray (EDX) measurements on NF extracted from NFA MA957, reported by Sakasegawa et al., indicate that they are non-stiochiometric $Y_2Ti_2O_7$, with Y/Ti < 1.0 for precipitates in the larger size range from up to 15 nm and Y/Ti ≈ 0.5 for the smallest pyrochlore features [3]. At largest sizes, from ≈ 15 to 35 nm, the oxides are closer to stiochiometric, with

Y/Ti ≈ 1.0. Yamashita et al. also found non-stiochiometric $Y_2Ti_2O_7$, but generally with a range of Y/Ti slightly greater than 1 [4,5]. Klimiankou et al. found near stoichiometric $Y_2Ti_2O_7$ in a 9Cr NFA using electron energy loss spectroscopy, HRTEM-fast Fourier transform (FFT) power spectra indexing and energy filtered TEM (EFTEM) methods [6,7]. Early x-ray diffraction (XRD) studies by Okuda and Fujiwara also indicated the presence of $Y_2Ti_2O_7$ in a 14Cr model NFA [8]. This observation has been confirmed by Sasasegawa et al., based on XRD measurements of nanopore filtered oxides extracted from a 9 Cr martensitic alloy [8]. Recently, Yu et al. reported a comprehensive TEM characterization study of NFA MA957 in different conditions, using various techniques [9]. This work clearly showed that extracted NF are structurally consistent with $Y_2Ti_2O_7$ and generally are near stoichiometric with Y/Ti ratios from 0.5 to 1. The dominant in-foil interface was found to be parallel to the {100} planes in Fe, although the oxide themselves could not be indexed. Note this paper also discusses some other recent work in the literature that did not find the pyrochlore $Y_2Ti_2O_7$. Finally, a recent high resolution TEM (HRTEM) study by Cisten et al confirmed that the in-foil NF in the same friction stirred weld variant of MA957 are $Y_2Ti_2O_7$ [10]. The study on the TEAM 0.5 showed that the dominant NF in-foil interface OR is $(100)_{Matrix}||(100)_{Y2Ti2O7}$ and $[001]_{matrix}||[1\text{-}10]_{Y2Ti2O7}$.

The high density of NF traps He in fine bubbles [11] and pin dislocations. The NF is also remarkably thermally stable [12,13]. However, the details of important processes (mechanisms and energies), such as helium trapping, are not well understood. Thus, while they may differ from those for embedded NF, creating a variety of mesoscopic surrogates, with self-selected sets of ORs with bcc Fe, will facilitate developing a general understanding of these metal-oxide interfaces in NFA, especially with respect to their structures and functional properties.

PROGRESS AND STATUS

Experimental Methods

A pure single crystal of $Y_2Ti_2O_7$ was acquired from McMaster University. The crystal was grown using a two-mirror NEC floating zone image furnace. The starting materials for the polycrystalline rods were 99.999% pure Y_2O_3 and 99.995% pure TiO_2, both from Alfa Aesar. The feed rods were created in the same fashion as Gardner [14]. The final single crystal was grown using the floating zone technique at a speed 5 mm/hr in air [15].

A 1.8 mm thick $Y_2Ti_2O_7$ single crystal wafer was cut to have a {111} oriented surface. A wire saw was used to cut a 2 mm thick {100} oriented $Y_2Ti_2O_7$ wafer. An Allied Multiprep system was used to polish the wafers using a sequence of 15 (for flattening), 9, 6, 3, and 1 μm papers for 10 minutes each at 75 rpm. The final 15 minute polishing step used a 0.02 μm non-crystallizing silica suspension. An electron beam system was used to deposit Fe on the $Y_2Ti_2O_7$ crystals at 7×10^{-6} torr and 800°C. The deposition rate was 2 nm/s for 250 s, producing Fe layer thicknesses of ≈ 500 nm. The samples were then slowly cooled to room temperature at a rate of ≈ 0.16°C/s.

An XPERT MPD Thin Film Texture XRD was used to obtain gonio scans and pole figures (PFs). A MFP-3D AFM was used to measure the topology of surfaces. A FEI Quanta 400F field-emission environmental scanning electron microscope (SEM) with an electron backscatter diffraction (EBSD) detector was used to obtain the inverse and Euler PFs and maps. A FEI HELIOS Focused Ion Beam (FIB) tool was used to micromachine <30-nm-thick electron transparent lift-outs of the interface Fe-$Y_2Ti_2O_7$ interfaces. Platinum was deposited over the Fe

for protection, and a low energy gallium beam with 2 keV 5.5 pÅ was used as a final sample-cleaning step.

Results and Discussion

Initial Study

Results from Fe depositions onto pyrex glass and onto an $Y_2Ti_2O_7$ single crystal wafer, which was 5 degrees miscut from the {111} surface, were previously reported. For these samples, the Fe was deposited at 0.3 nm/sec. Deposits of Fe on a pyrex glass substrate were used to provide a naturally selected Fe grain OR for an amorphous control surface. AFM measurements showed the deposit is characterized by many Fe polycrystals with average grain size of 1 μm and a surface roughness of about 40 nm. XRD scans showed that the grains have a {110} out of plane texturing with no in-plane OR.

Figure 1 has been reproduced from Reference [17]. Figure 1(a) shows the EBSD inverse pole figures (PFs) from the miscut $Y_2Ti_2O_7$ substrate. The two PFs in Figure 1(a) show spots that were expected from a good quality single crystal with a {111} orientation. Figure 1(b) shows a SEM image of Fe grown on the miscut {111} $Y_2Ti_2O_7$ single crystal substrate. The topography of the Fe film is similar to that of the Fe found on the control sample. Some grains coalesced and formed larger islands, while others remained as isolated grains.

The EBSD inverse pole map in Figure 1(c) shows the out-of-plane crystallographic orientation of the Fe grains in Figure 1(b). Each of the Fe crystallographic surface orientations is assigned an individual color, which is shown in the octant at the top right of Figure 1(c). Most Fe grains are either {110} oriented (green) or {100} oriented (red). A few grains (yellow) have an orientation between {100} and {110}, and a few grains (light blue/purple) have an orientation between {110} and {111}. Overlaying Figures 2(b) and (c) shows that some {110} Fe grains and some {100} Fe grains remained as isolated islands, while both like and unlike grains frequently coalesced. Figure 1(d) shows the same crystallographic information about the Fe grains as Figure 1(c), but represented as PFs.

The in-plane Fe-$Y_2Ti_2O_7$ ORs are obtained by comparing the spots from each Fe PF in Figure 1(d) to each $Y_2Ti_2O_7$ PF in Figure 1(a). The following Fe to $Y_2Ti_2O_7$ crystallographic ORs are observed:

OR1: $\{110\}_{Fe} \parallel \{111\}_{Y2Ti2O7}$ and $\langle 100\rangle_{Fe} \parallel \langle 110\rangle_{Y2Ti2O7}$
OR2: $\{100\}_{Fe} \parallel \{111\}_{Y2Ti2O7}$ and $\langle 100\rangle_{Fe} \parallel \langle 110\rangle_{Y2Ti2O7}$

Notably, OR1 is the Nishiyama Wasserman (NW) orientation relationship. Figure 1(e) derives from the same EBSD scan as Figures 2(c) and (d), but shows the orientations of the Fe grains represented as an Euler map. The full crystallographic orientation of each grain is assigned a color that is associated with a series of three rotations around three Euler axes. The crystallographic information from the Euler map is also represented in the Euler PFs in Figure 1(f). The colors in the Euler PFs match the grain colors in the Euler map. Figure 1(f) shows that the three in-plane orientations of the {110} and {100} Fe grains match the threefold symmetry of the {111} $Y_2Ti_2O_7$ substrate planes. Sketches of the substrate orientation and of the grain orientations are shown in Figure 1(g). The colors of the grains in Figure 1(g) match

the colors of the grains in the Euler map and in the Euler PFs. In conclusion, most Fe grains were epitaxially grown on the $Y_2Ti_2O_7$ substrate with two ORs.

Effect of Deposition Rate

The effect of Fe deposition rate was studied by first removing the Fe grains from the 5 degree miscut {111} $Y_2Ti_2O_7$ sample. This was done by polishing away the grains in the same fashion as described previously. Fe was then deposited at a rate of 2 nm/s, nearly seven times faster than in the initial study. Figure 2(a) shows the EBSD inverse pole figure map from the initial study. Figure 2(b) shows the out of plane orientation of the faster deposited Fe film. The faster deposition clearly shows grains with a dominant {110} texturing. The PFs in Figure 2(c) are from the initial study while the PFs in Figure 2(d) are from the faster deposition. Figure 2(d) confirms that there is strong $\{110\}_{Fe}$ texturing. The PFs do not have the red spots as seen in Figure 2(c), thus the {100} Fe grains were not present. The {110} Fe grains still matched the underlying substrate three-fold symmetry. In conclusion, the faster deposition rate prevented grains with OR2.

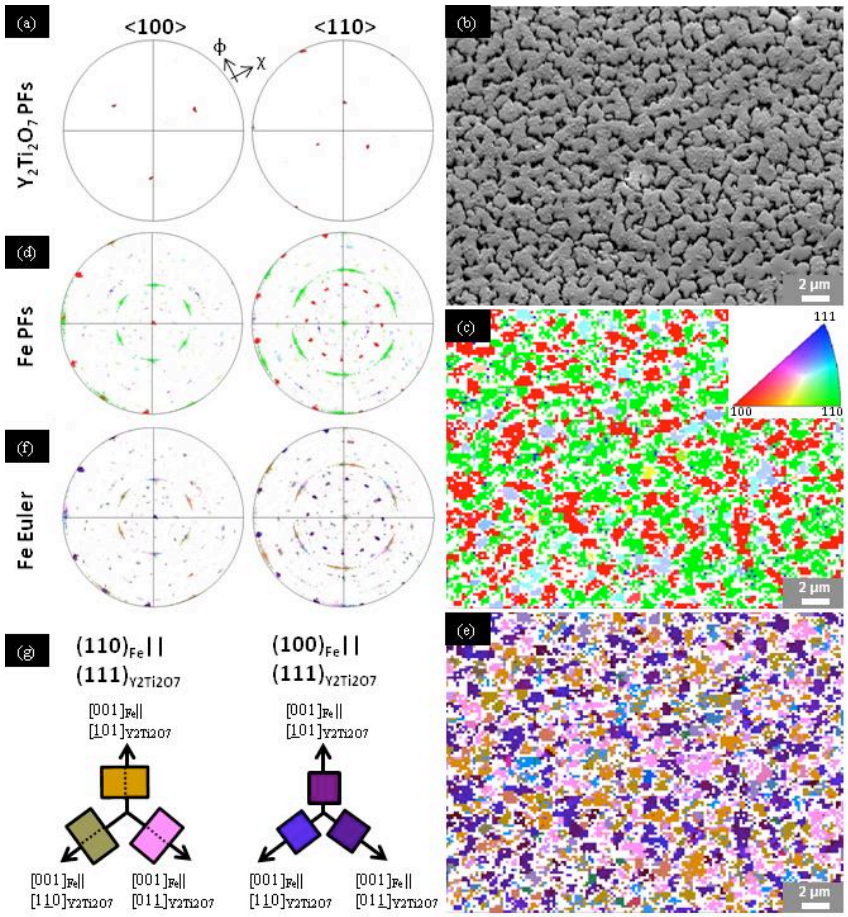

Figure 1. This figure has been reproduced from reference [17]. (a) EBSD PFs of the $Y_2Ti_2O_7$ substrate showing a good quality {111}-oriented single crystal. (b) SEM of Fe grains on the $Y_2Ti_2O_7$ single crystal substrate. Some Fe grains coalesced, while some Fe grains remained as single islands. (c) EBSD inverse pole map of the Fe grains on the $Y_2Ti_2O_7$ substrate. The octant in the top right indicates the surface orientations of the Fe grains. (d) PFs of the grains showing reflections from $\{110\}_{Fe}$ in green and $\{100\}_{Fe}$ in red. (e) Euler map showing the full crystallographic orientation of the grains. (f) Euler PFs showing the crystallographic orientation of each grain. (g) Schematic showing how the $<100>_{Fe}$ directions match the three <110> directions of the {111} substrate. The colors in the schematic match the colors in (f) and (g).

Effect of Miscut Angle

The previous two depositions were done on an $Y_2Ti_2O_7$ wafer, which was 5 degrees miscut from the {111} plane. The effect of miscut angle was studied by creating a new $Y_2Ti_2O_7$ substrate with an orientation less than 1 degree off from the {111}. This was done by using x-ray diffraction to determine the {111} planes, cutting a wafer using a diamond wire saw, and polishing the wafer using the same procedure described previously. Fe was deposited using the fast deposition rate of 2 nm/sec. EBSD scans are seen in Figure 3(a) and show that the grains were larger than in the previous studies. The blue, purple, and red areas in Figure 3(a) show tall, pillar-like, grains that have a random OR with the substrate. The PFs in Figure 3(b) show that the grains are $\{110\}_{Fe}$ textured with OR1. The miscut angle did not affect the OR of most of the grains, but did affect the size.

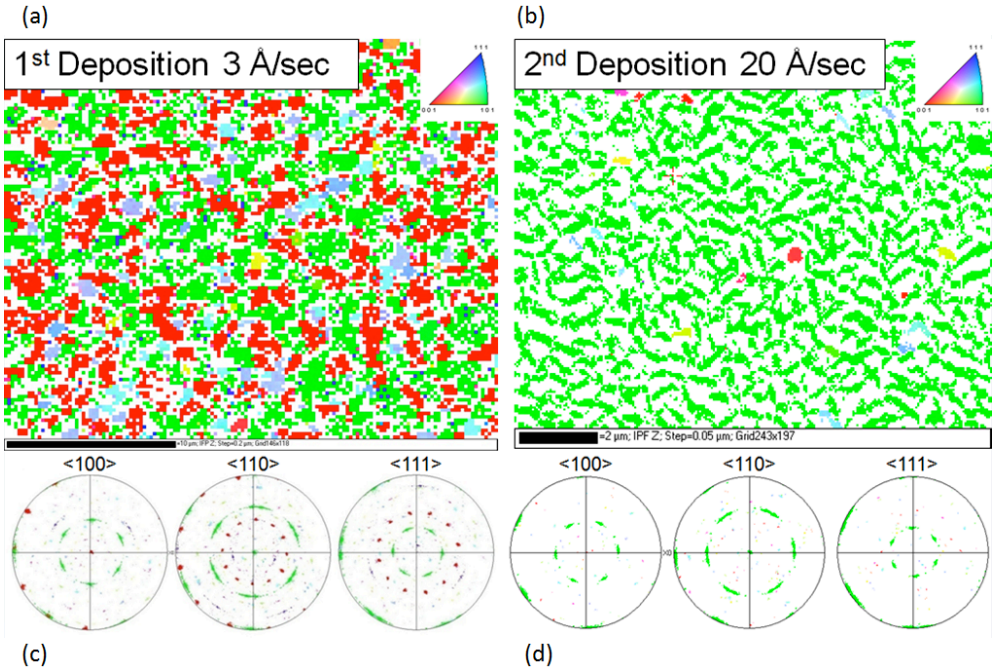

Figure 2. EBSD inverse pole figure maps from the slow deposition (a) and from the fast deposition (b) show that there are more $\{110\}_{Fe}$ grains in the fast deposition. PFs from the slow deposition (c) and from the fast deposition (d) show that the $\{110\}_{Fe}$ grains match the underlying three-fold symmetry of the substrate.

Effect of Orientation

A {100} $Y_2Ti_2O_7$ single crystal wafer was used to investigate the effect of substrate orientation. Fe was deposited using the fast deposition rate of 2 nm/sec. Figure 4(a) shows the out of plane orientation of the Fe grains. The grains are similar in size as the previous depositions, and are strongly {110} textured. The dark rings in the PFs in Figure 4(b) show that the Fe grains do not have an out of plane OR with the substrate. This is identical to the depositions on amorphous pyrex. The {100} oriented $Y_2Ti_2O_7$ substrate did not affect the growth of the Fe grains.

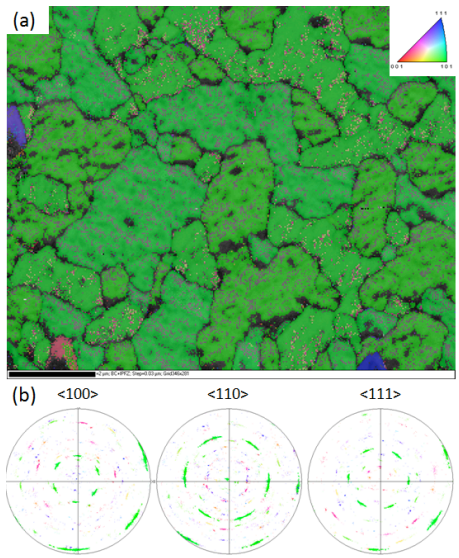

Figure 3. EBSD out of plane orientations of Fe grains are shown in (a). Pole figures in (b) show that the Fe grains are of the OR1 type.

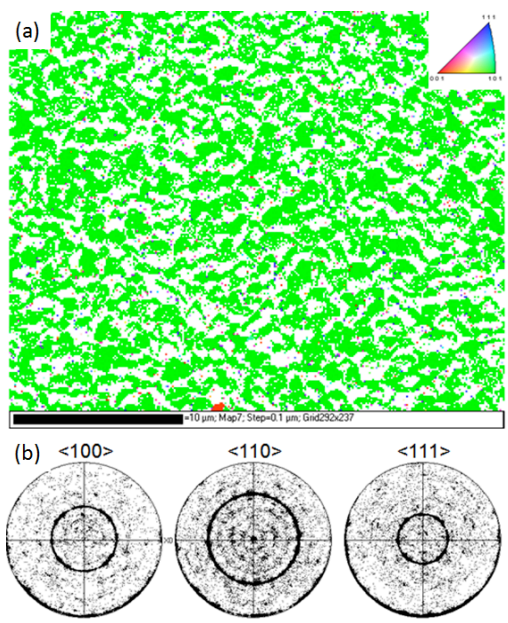

Figure 4. EBSD out of plane orientations of Fe grains are shown in (a). Pole figures show that the Fe grains do not have an out of plane orientation relationship with the {100} $Y_2Ti_2O_7$ substrate.

TEM Characterization of Initial Study

A detailed cross-sectional TEM and HRTEM study was conducted to explore the structure of the Fe-$Y_2Ti_2O_7$ interfaces. Figure 5 has been reproduced form reference [17]. The cross-sectional TEM micrographs in Figures 5(a) and (b) show the island type growth of the Fe on the 5 degree

miscut $Y_2Ti_2O_7$ substrate. Figure 3(c) illustrates the crystallographic orientations of the grains and substrate. There does not seem to be a correlation between a grain's shape and its crystallographic orientation.

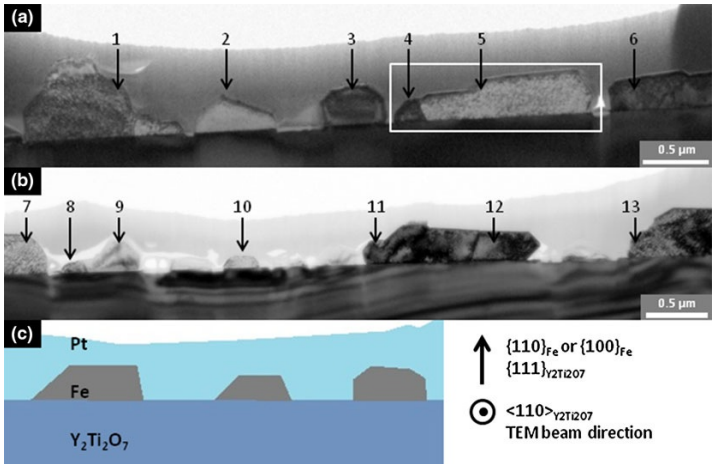

Figure 5. This figure was reproduced from reference [17]. (a), (b) Cross-sectional TEM images of Fe grains on the {111} $Y_2Ti_2O_7$ substrate. (c) Sketch of (a) and (b) showing the crystallographic orientation of the grains and substrate.

HRTEM was used to closely examine the interfaces between grains and the substrate. Figure 6 has been reproduced from reference [17]. Figure 6(a) shows the interface structure that is typical of NW OR1 grains. This interface is sharp and flat at the near-atomic scale. The substrate $\{111\}_{Y2Ti2O7}$ planes are visible and marked by red lines in Figure 6(a). The termination of red lines at ledges accommodates the 5 deg surface miscut from $\{111\}_{Y2Ti2O7}$. The light and dark regions about 8 nm apart coincide with the ledges and indicate that there is stress at the interface.

Figure 6(b) shows a HRTEM image of the interface between the substrate and a grain with OR2. There is a 2 to 3-nm-thick transition layer at the interface. The STEM/EDX spectrum in Figure 6(c) shows that the transition layer is rich in Ti, O, and Fe and is consistent with a MO_x metallic oxide. However, the exact composition of the transition layer has not been measured. Figure 7 shows the interface of a Fe grain with no clear OR with the $Y_2Ti_2O_7$ substrate. The interface is atomically rough and incoherent. The 5 nm thick uneven dark areas at the interface is probably also a MO_x transition layer. Grains with no OR generally have thicker MO_x transition layers than grains with OR2.

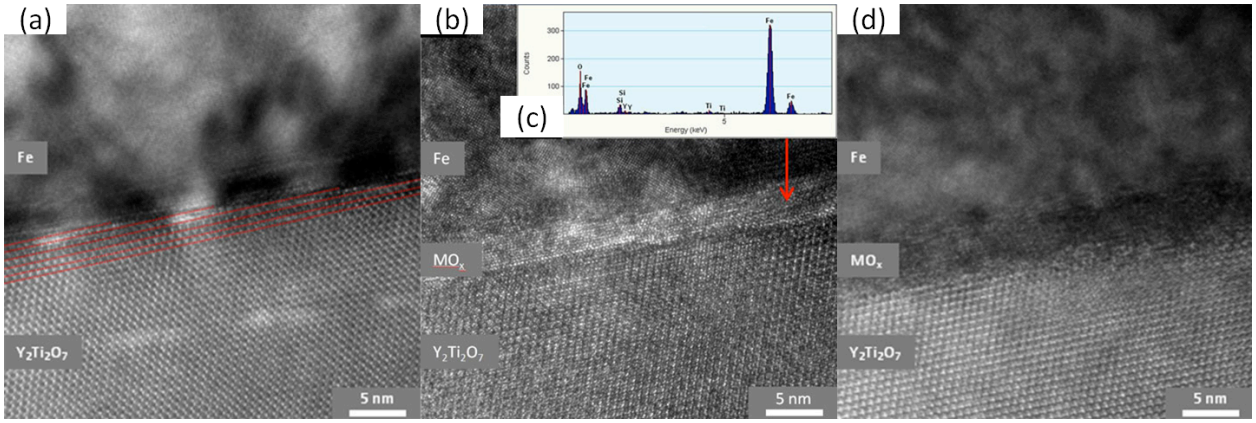

Figure 6. HRTEM image from a grain with the NW OR1. The red lines show {111}$Y_2Ti_2O_7$ planes. Dark and light strained areas are seen at substrate ledges. (b) HRTEM image showing the MO_x interfacial transitionnal layer found between a Fe grain and the $Y_2Ti_2O_7$ substrate with the OR2. (c) An EDX spectrum taken from the transition layer in (b). (d) The interface of Fe grains with no OR to the substrate. A thick MO_x transition layer is seen at the Fe-$Y_2Ti_2O_7$ interface.

Effect of Deposition Rate

A TEM scan of the fast deposition on the miscut {111} $Y_2Ti_2O_7$ is shown in Figure 7(a). The grains coalesced and did not remain as isolated islands as seen in the slow deposition. Figure 7(b) is an HRTEM scan the Fe-$Y_2Ti_2O_7$ interface for a grain with NW OR1. The red lines show the {111} $Y_2Ti_2O_7$ planes and their termination at the interface. Similar to the slow deposition, this interface is characterized by light and dark strained regions, which coincide with the {111} plane terminations. A MO_x transition layer is not seen at the interface.

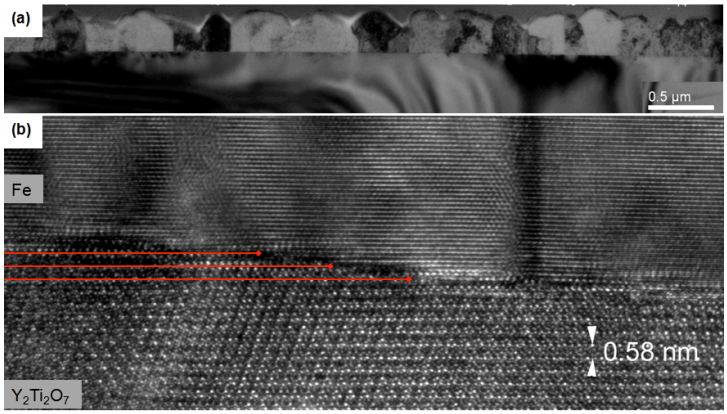

Figure 7. TEM image of Fe grains from the fast deposition rate are shown in (a). HRTEM image of the Fe-$Y_2Ti_2O_7$ interface with OR1 is shown in (b).

Effect of Miscut Angle

Figure 8(a) shows the Fe grains grown on the well oriented {111} $Y_2Ti_2O_7$ substrate. The grains coalesced together into one thin film. There are also white pillar-like grains that are taller than the rest of the film. Diffraction patterns from these grains (not shown) indicate that the grains

have no OR with the substrate. Figure 8(b) shows an HRTEM image of the Fe- $Y_2Ti_2O_7$ interface with NW OR1. The interface is clean and sharp, without the alternating dark and light regions seen in the miscut samples. Some grains show a nano Fe grain (up to 6 nm tall and 10 nm wide) that nucleated at the interface, but did not grow. The nano grains have the same NW OR1 as the surrounding larger grain, but are generally slightly rotated in plane (by 1 degree).

Continuing and Future Research

This work is continuing and will be extended to other oxide surface orientations and different deposition conditions will also be explored. TEM was not done on the depositions on {100} $Y_2Ti_2O_7$ since the Fe grains had no in-plane OR with the substrate. However, we are trying to obtain the $\{100\}_{Y2Ti2O7}$ || $\{100\}_{Fe}$ and $<110>_{Y2Ti2O7}$ || $<100>_{Fe}$ interface by diffusion bonding single crystals of Fe and $Y_2Ti_2O_7$. The {100} Fe and {100} $Y_2Ti_2O_7$ crystals were cut, polished, and matched together to have the desired OR. Attempts to diffusion bond the crystals at a temperature of 700 degrees C for 10 hours and 10 MPa have so far been unsuccessful. We are still exploring different diffusion bond parameters and conditions. There will also be studies of the interface interactions with irradiation induced defects and helium.

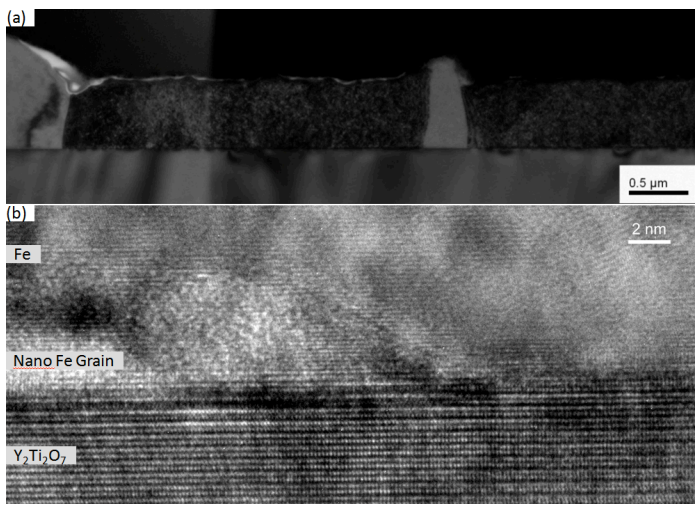

Figure 8. The TEM cross-section image from the Fe-$\{111\}_{Y2Ti2O7}$ interface is seen in (a). The HRTEM image in (b) shows a nano grain, which was sometimes found at the interface.

ACKNOWLEDGEMENTS

The authors thank Erin Haney, Gareth Seward, Mark Cornish, Deryck Stave, Youli Li, and Doug Klingensmith for help with various parts of the research. The work performed at UCSB was supported by the U. S. Department of Energy, Office of Fusion Energy Sciences, under grant DE-FG03-94ER54275.

REFERENCES

[1] G. R. Odette, M. J. Alinger, and B. D. Wirth, *Annu. Rev. Mater. Res.* **38** (2008) 471.
[2] Y. Dai, G. R. Odette, and T. Yamamoto, *Comp. Nucl. Mater.* **1** Chap. 6 (2012) 141.
[3] H. Sakasegawa, L. Chaffron, F. Legendre, et al., *J. Nucl. Mater.* (2009) 384.
[4] S. Yamashita, S. Ohtsuka, N. Akasaka, et al., *Phil. Mag. Lett.* (2004) 84.
[5] S. Yamashita, N. Akasaka, and S. Ohnuki, *J. Nucl. Mater.* (2004) 329.
[6] M. Klimiankou, R. Lindau, and A. Möslang, J. *Nucl Mater.* (2004) 329.
[7] M. Klimiankou, R. Lindau, and A. Möslang, *Micron* (2005) 36.
[8] T. Okuda and M. Fujiwara, *J. Mater. Sci. Lett.* (1995) 14.
[9] Y. Wu, E. M. Haney, N. J. Cunningham, et al., *Acta Mater.* **60** (2012) 3456.
[10] J. Ciston, Y. Wu, G. R. Odette, et al., *Fus. Mat. Semiann. Prog. Rep.* (2012) DOE-ER-0313/51.
[11] G. R. Odette, et al., *J. Nucl. Mat.* (2011).
[12] S. Y. Zhong, J. Ribis, V. Klosek, et al., *J. Nucl. Mater.* **12** (2012).
[13] M. J. Alinger, G. R. Odette, and D. T. Hoelzer, *J. Nucl. Mater.* (2004) 382.
[14] J. S. Gardner, B. D. Gaulin, and D. M. Paul, *J. Cryst. Grow.* **191** (1998) 740.
[15] M. B. Johnson, H. A. Dabkowska, B. D. Gaulin, et al., *J. Solid State Chem.* **182** (2009) 725.
[16] A. Hashibon, A. Y. Lozovoi, and P. Gumbsch, *Phys. Rev. B* **77** (2008) 094131.
[17] T. Stan, Y. Wu, G. R. Odette. et al., *Metal. Mater. Trans. A*, Currently Online Only (2013).